

Quasiparticle self-consistent GW electronic band structures of Be-IV- N_2 compounds

Sai Lyu and Walter R. L. Lambrecht

*Department of Physics, Case Western Reserve University,
10900 Euclid Avenue, Cleveland, Ohio 44106-7079, USA*

The electronic band structures of BeSiN₂ and BeGeN₂ compounds are calculated using the quasiparticle self-consistent GW method. The lattice parameters are calculated for the wurtzite based crystal structure commonly found in other II-IV- N_2 compounds with the $Pbn2_1$ space group. They are determined both in the local density approximation (LDA) and generalized gradient approximation (GGA), which provide lower and upper limits. At the GGA lattice constants, which gives lattice constants closer to the experimental ones, BeSiN₂ is found to have an indirect band gap of 6.88 eV and its direct gap at Γ is 7.77 eV, while in BeGeN₂ the gap is direct at Γ and equals 5.03 eV. To explain the indirect gap in BeSiN₂ comparisons are made with the parent III-N compound w-BN band structure. The effective mass parameters are also evaluated and found to decrease from BeSiN₂ to BeGeN₂.

I. INTRODUCTION

BeSiN₂ and BeGeN₂ form part of a larger family of II-IV- N_2 nitrides, which can be viewed as derived from the III-N family by replacing two of the group-III atoms in each tetrahedron surrounding the N by a group-II atom and two by a group-IV atom. By expanding the family of group-III nitrides including these heterovalent ternaries, significant new opportunities for band structure engineering and materials property design are opened. The occurrence of two different valence cations in these structures presents new challenges in terms of stoichiometry control, understanding the possible disorder effects, and more complex defect physics but also offers new possibilities in combination with existing nitrides exploiting band-offsets between lattice matched pairs of compounds. For an overview of this materials family and related recent work, see Refs. 1–3.

The special interest in Be as group II element arises from it being a second row element in the periodic table. This makes the related compounds closely related to BN, the III-N parent compound. BN itself is an interesting material usually found in a layered form similar to graphite, and known as hexagonal or h-BN. However, at high pressures a tetrahedrally bonded form exists, which is usually found in the cubic zincblende polytype. Nonetheless there also exists a hexagonal tetrahedrally bonded form with the wurtzite structure. Both these forms are considered extremely hard materials comparable to diamond in their properties. The atmospheric pressure form however is graphite like and involves trigonal bonding because of π -bonding between the second row elements B and N. By replacing B with Be and Si or Be and Ge we may preserve some of the unique properties of BN and at the same time favor the tetrahedral bonding resulting in extremely hard and wide band gap materials.

BeSiN₂ and BeGeN₂ are expected to have among the highest band gaps in this family of materials and could thus be useful for optical devices with wavelengths in the ultraviolet region. Synthesis of BeSiN₂ and its crystal

structure were reported by Eckerlin *et al.* in 1967.^{4,5} The structural properties and electronic band structures at the level of density functional theory (DFT) of BeSiN₂ and BeGeN₂ were reported by Huang *et al.*⁶ and Shaposhnikov *et al.*⁷ However, DFT in the local density approximation (LDA) is well known to underestimate the band gaps for semiconductors. A more accurate method is needed to predict the electronic properties of the Be-IV- N_2 compounds, which have not yet been determined experimentally. Here we present a study of the band structures using the quasiparticle self-consistent GW method,⁸ which provides excellent agreement with experimental band gaps for most tetrahedrally bonded semiconductors. The goals of this work are to predict accurate band gaps, valence band fine structure and effective masses of these materials and to provide and understanding of the direct or indirect nature of the gaps. The details of the computational methodology used here can be found in section II. The structural properties are given in section III A, and the discussion on stability is in III B. The electronic band structures are shown in section III C, and the effective masses in section III D. We summarize the main results in section IV.

II. COMPUTATIONAL METHOD

The structural properties are obtained via the Broyden-Fletcher-Goldfarb-Shanno (BFGS) minimization method⁹ using the ABINIT package¹⁰ in both local density approximation(LDA) and generalized-gradient approximation in the Perdew-Burke-Ernzerhof form(PBE-GGA)¹¹ within the general context of density functional theory. The BFGS method allows one to optimize the cell shape and atomic positions simultaneously because it makes use of the stress tensor and hence gradients are available for the total energy with respect to atomic displacements as well as the lattice constants defining the shape and volume of the unit cell. The interaction between valence electrons and ions are described using a pseudopotential. To be more specific, we used the Hartwigsen-Goedecker-Hutter (HGH)¹² pseu-

dopotentials in LDA and Fritz-Haber-Institute (FHI)¹³ pseudopotentials in GGA. The wave functions are expanded in a plane wave (PW) basis set with energy cutoff of 100 Hartree and a $4 \times 4 \times 4$ \mathbf{k} -point mesh sampling of the Brillouin zone is used. The forces are relaxed to be less than 5×10^{-5} Hartree/Bohr.

Next, the density functional theory (DFT)¹⁴ band structures are calculated using the full-potential linearized muffin-tin orbital (FP-LMTO) all-electron method.^{15–17} This provides a check on the pseudopotential band structures with a method that does not require pseudopotentials. In the FP-LMTO calculations, we used a double- κ basis set where κ denotes the decay length of the spherical wave basis function envelopes, which are smoothed Hankel functions. These are then augmented inside the spheres in spherical harmonics up to $l = 4$ times radial functions and their energy derivatives corresponding to the actual all-electron potential inside the spheres. Specifically, *spd* – *sp* on Be atom and *spdf* – *spd* on other atoms are included in the basis set. The Ge-3*d* were treated as bands using local orbitals. The Brillouin zone was sampled using a $6 \times 8 \times 8$ \mathbf{k} -point mesh.

This DFT band structure is used as the starting point for the quasiparticle self-consistent (QS) *GW* method.^{8,18} The *GW* method is a many-body perturbation theoretical method first introduced by Hedin.^{19,20} In this method, the complex and energy dependent self-energy $\Sigma(\omega)$ describes the dynamic interaction effects beyond the DFT level self-consistent field. In the *GW* approximation it is given in terms of the one-electron Green's function $G(12)$ and the screened Coulomb interaction, $W(12)$, as $\Sigma(12) = iG(12)W(1^+2)$, where 1 is a short hand for the position, spin and time of particle 1 and 1^+ indicates a time infinitesimally after t_1 . The screened Coulomb interaction is itself obtained from the Green's function via $P(12) = -iG(12)G(21)$ and $W = [1 - vP]^{-1}v$, where v is the bare Coulomb interaction and W the screened one. All of these equations are in fact solved after Fourier transformation to \mathbf{k} -space and energy ω and in a basis set of auxiliary Bloch functions, which consists of product functions of muffin-tin orbitals inside the spheres and interstitial plane waves. But the above real-space and time notation just provides the most concise way of stating the method's approximations. Details of the basis set implementation in terms of muffin-tin orbitals are provide in Ref.18

In the QSGW method,¹⁸ the energy dependent self-energy matrix in the basis of the independent electron Hamiltonian (LDA) eigenstates is replaced by an energy averaged and Hermitian matrix

$$\tilde{\Sigma}_{ij} = \frac{1}{2} \text{Re}\{\Sigma_{ij}(\epsilon_i) + \Sigma_{ij}(\epsilon_j)\} \quad (1)$$

This then replaces the starting LDA (or GGA) exchange-correlation potential and defines a new independent particle Hamiltonian H_0 whose eigenvalues and eigenstates provide a new G_0 and through the next G_0W_0 calcula-

tion the next $\tilde{\Sigma}$. The process is then iterated till the self-energy $\tilde{\Sigma}$ is self-consistent at which point the Kohn-Sham eigenvalues of H_0 coincide with the quasiparticle excitation energies of the many-body theory. Hence the name quasiparticle self-consistent *GW*. Note that in the process the eigenfunctions are recalculated in each step by re-diagonalizing the H_0 of that iteration which includes the $\tilde{\Sigma}$ instead of the original v_{xc} from the previous step. The details of the implementation of the QSGW method and various technical aspects can be found in Ref. 18. In the present QSGW calculation, the $\Sigma(\omega)$ is calculated up to $\omega = 2.5$ Ry, and is approximated by a diagonal average matrix when it is above 2 Ry before calculating the quasiparticle shifts in the next step. A cut-off of 3.5 Ry is used for the interstitial plane-waves and for the Coulomb interactions auxiliary basis set. The \mathbf{k} -point mesh over which the *GW* self-energy is evaluated was set as $3 \times 3 \times 3$. The Σ is at this point known as a matrix in the basis of H_0 eigenstates $\psi_{n\mathbf{k}}$. Expanding these in the basis set of muffin-tin orbital Bloch functions $\chi_{RL\mathbf{k}}$, and subsequently each of these into $\chi_{RL\mathbf{T}}$ by an inverse Bloch sum (or discrete Fourier transform) the $\tilde{\Sigma}_{RL,R'+\mathbf{T}L'}$ is then obtained in real space up to a certain range. Here, R denotes the site in the unit cell, L the angular momentum and other indices needed to specify the specific basis function centered at this site, and \mathbf{T} the lattice vectors. This can now be converted back by a direct Bloch sum to the $6 \times 8 \times 8$ \mathbf{k} -point set used for the charge self-consistency iterations of H_0 and eventually also to the \mathbf{k} -points along symmetry lines of the Brillouin zone for the band structure plots. This effective interpolation scheme allows us to obtain the bands at the *GW* level at any \mathbf{k} -point and hence also accurate effective masses. It is essentially equivalent to a Wannier function interpolation scheme, except that in the LMTO approach we do not need to construct Wannier functions because we already have a relatively short-range atom centered basis set.

Finally, we note that in the QSGW approximation, the screening of the Coulomb interactions is usually found to be underestimated by about 20 %, ^{21,22} resulting in band gaps being overestimated. This can be corrected by mixing 80% of the $\tilde{\Sigma}$ with 20 % of the original LDA v_{xc}^{LDA} and is referred to as the 0.8 Σ approximation. We note that this may sound similar to a hybrid functional but is in practice quite different because there is no adjustment of this fraction involved and this represents in effect going beyond standard *GW* by including additional diagrams in the calculation of W which could now in fact be done explicitly following the Bethe-Salpeter Equation (BSE) approach,²³ but at a much higher cost than the standard QSGW + 80 % renormalization. In other words, where the calculations have been done at this beyond standard *GW* level, for example using a time dependent DFT (TDDFT) approach with an exchange correlation kernel in the screening of W extracted from BSE,^{24,25} they tend to confirm the 80% renormalization approach as analyzed in Ref. 22.

TABLE I. Calculated lattice parameters of Be-IV-N₂ compared with experimental values.

Compound	method	$a(\text{\AA})$	$b(\text{\AA})$	$c(\text{\AA})$	$V(\text{\AA}^3)$	b/a_w	c/a_w
BeSiN ₂	LDA	5.67	4.92	4.62	128.9	1.74	1.63
	GGA	5.75	4.98	4.68	134.0	1.73	1.63
	Expt. ^a	5.747	4.977	4.674	133.7	1.73	1.63
	LDA ^b	5.697	4.939	4.639	133.7	1.73	1.63
	GGA ^b	5.772	4.999	4.699	135.6	1.73	1.63
BeGeN ₂	LDA	5.81	5.07	4.77	140.5	1.75	1.64
	GGA	5.93	5.17	4.86	149.0	1.74	1.64
	LDA ^b	5.856	5.105	4.803	143.6	1.74	1.64
	GGA ^b	5.972	5.204	4.894	152.1	1.74	1.64

^a From Eckerlin⁵

^b From Shaposhnikov *et al.*⁷

III. RESULTS

A. Crystal structure

The calculated lattice constants for BeSiN₂ and BeGeN₂ in both LDA and GGA are given in Table I. The space group is $Pbn2_1$ and the order of the lattice constants is chosen so that $a > b$. The relation of the lattice constants in the idealized orthorhombic structure to those in the wurtzite structure is given by $a = 2a_w$, $b = \sqrt{3}a_w$ and $c = c_w$. The optimized b/a_w ratio indicates how far the structure is from the idealized wurtzite structure. From the results in Table I we can see that BeSiN₂ is closer to the idealized wurtzite structure than BeGeN₂. The GGA lattice constants are systematically larger than the LDA ones which is commonly found. We also compare our relaxed lattice constants with those reported in literature and with the experimental values for BeSiN₂. Good agreement is found. Only the experimental lattice constants of BeSiN₂ are available. In this case, we can see that GGA lattice constants are more accurate than LDA ones. Both LDA and GGA produce nearly the same b/a_w and c/a_w ratios in both materials studied here. The crystal structure of BeSiN₂ is shown in Fig. 1 and BeGeN₂ has a similar structure.

The atomic positions of the atoms in the unit cell are given in terms of Wyckoff 4a positions in Table II. The origin is set at the position of the 2-fold screw axis in the $xy = ab$ plane. We may note that the nitrogen atoms are sitting nearly on top of the Be and group-IV atoms which shows that BeSiN₂ has its orthorhombic crystal structure very close to the supercell of wurtzite without much distortion.

B. Formation energy and stability

We next check the thermodynamic stability. The energies of formation are calculated from the cohesive energies as given in Table III which are calculated in the

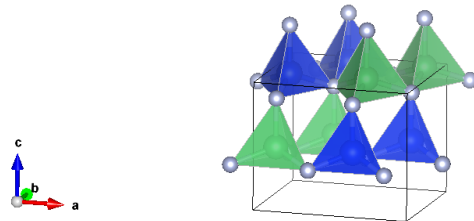
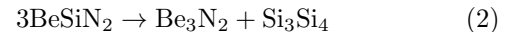


FIG. 1. Crystal structure of BeSiN₂. The small open spheres represent N atoms, the green and blue larger spheres inside the nearest neighbor tetrahedrons represent Be and Si respectively.

TABLE II. Wyckoff positions of Be-IV-N₂ in the GGA approximation.

Compound	atom	x	y	z
BeSiN ₂	Be	0.125	0.083	-0.013
	Si	0.625	0.086	-0.014
	N _{Be}	0.127	0.084	0.365
	N _{Si}	0.623	0.080	0.362
BeGeN ₂	Be	0.125	0.080	-0.013
	Ge	0.624	0.091	-0.013
	N _{Be}	0.115	0.072	0.351
	N _{Ge}	0.634	0.091	0.375

GGA approximation by subtracting the atomic energies from the solid's total energy. The atomic energies include the spin-polarization energy. The N₂ molecule was calculated in a large unit cell using the FP-LMTO method and including additional augmented plane wave basis functions¹⁶ to well represent the region outside the molecule, which is important to obtain total energies which are not sensitive to the choice of muffin-tin radii. The energies of formation of both compounds are negative, meaning that they are stable relative to the elements in their respective phases at standard conditions (room temperature and atmospheric pressure). They are also found to be stable relative to the competing binary compounds. The formation energies of the latter were calculated for the phases already found to be the minimum energy structures in the Materials Project²⁶ and compared with the data in that database in Table III. They show that the BeSiN₂ is stable against the reaction



by 0.136 eV/atom and similarly for the Ge case by 0.176 eV/atom.

C. Energy bands and density of states

The band structures and partial densities of states (PDOS) in the 0.8Σ QSGW approximation at GGA lat-

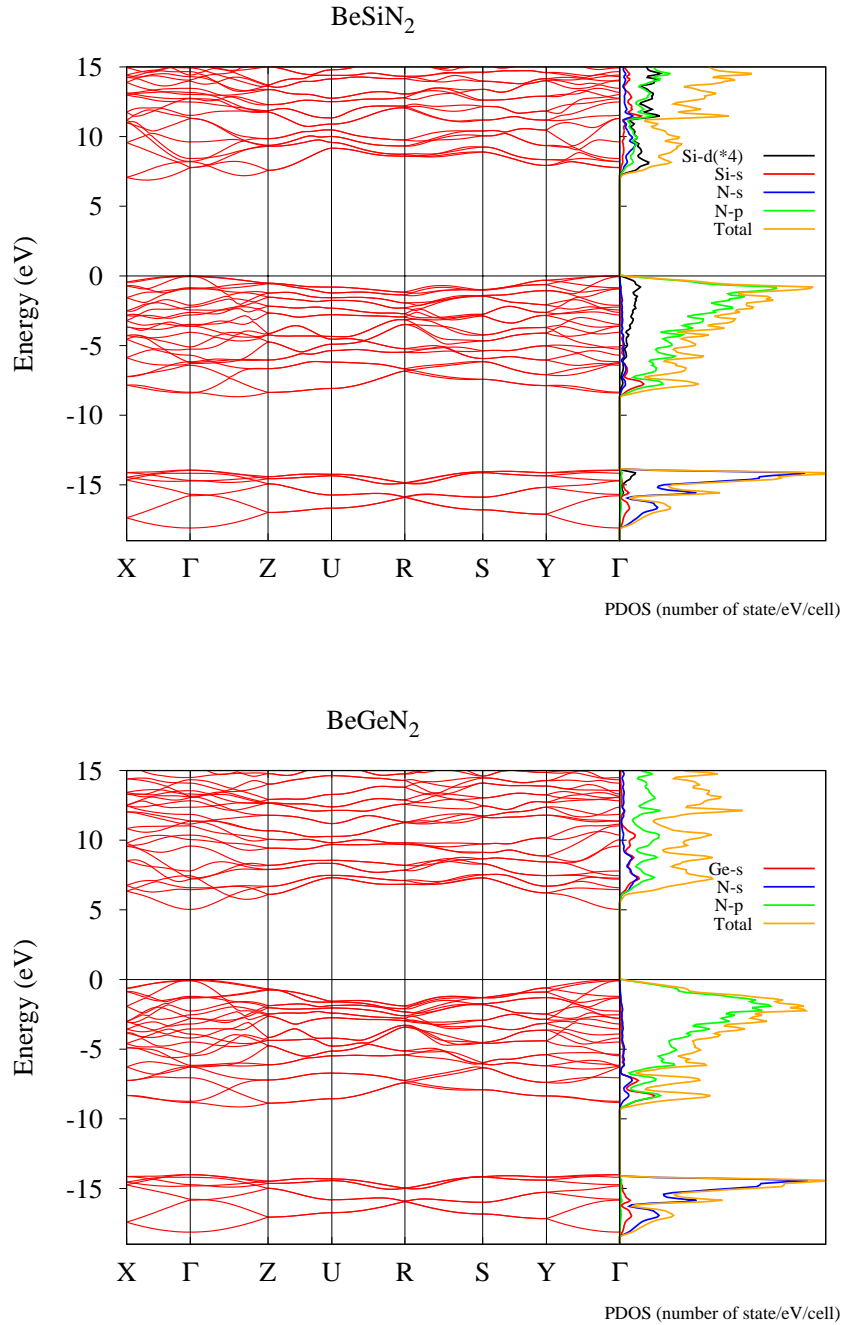


FIG. 2. Band structures and partial densities of states of BeSiN₂ and BeGeN₂ in the QSGW approximation at the GGA lattice constants.

tice constants are shown in Fig. 2. The PDOS show that, as expected, the lowest set of 8 valence bands near -15 eV are dominated by N-*s* and the next set of valence bands (between -9 eV and the VBM set at 0), by N-*p* orbitals. The conduction bands have more cation character but also N-*s* and N-*p* because the cation states are antibonding with the N-orbitals. In the case of BeSiN₂, we

see it has even a strong Si-*d* character. The conduction band orbital character will be analyzed in more detail in a **k**-resolved manner below.

BeGeN₂ is found to be a direct band gap semiconductor while BeSiN₂ has an indirect band gap. In BeGeN₂, both the CBM and VBM occur at the Γ point. An indirect band gap was previously also found for ZnSiN₂,²⁷

TABLE III. Cohesive energies and formation energies (in eV/atom) calculated in the PBE-GGA approximation.

	ours	MP ^a
Be	3.44	
Si	4.49	
Ge	3.39	
N	5.17	
Be ₃ N ₂	-1.24	-1.225
Si ₃ N ₄	-1.04	-1.312
Ge ₃ N ₄	-0.08	-0.26
BeSiN ₂	-1.26	-1.412
BeGeN ₂	-0.74	-0.813

^a Material Project²⁶

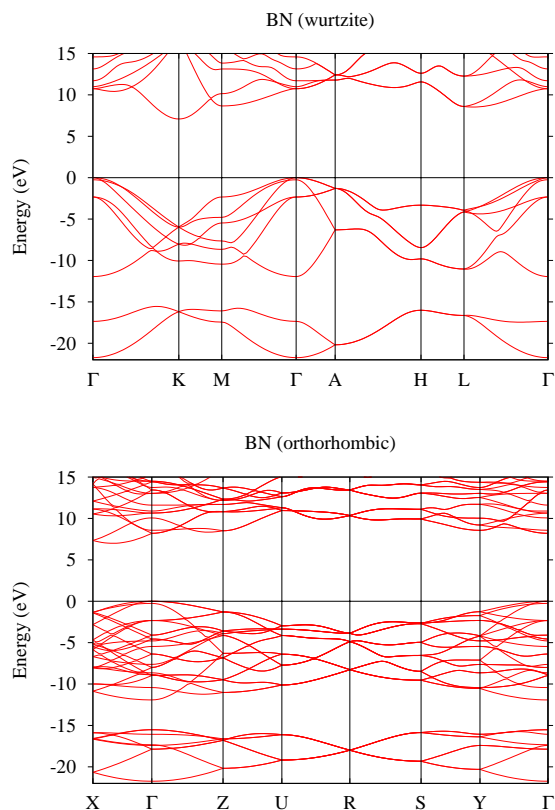


FIG. 3. Band structures of BN plotted in Brillouin zone of wurtzite and orthorhombic structure in the QSGW approximation.

MgSiN₂²⁸ and CdSiN₂²⁹. However, in those cases, the CBM is at Γ and the VBM near one of the Brillouin zone edges. On the other hand, in BeSiN₂, the VBM is at Γ but the CBM is located between the Γ and X points. In Ref. 7, the CBM for BeSiN₂ occurs between Γ and Y which is simply because of the difference in labeling. Their Y is actually labeled as X in the present work because the a and b axes are interchanged. This location of the CBM is robust and in agreement between LDA,

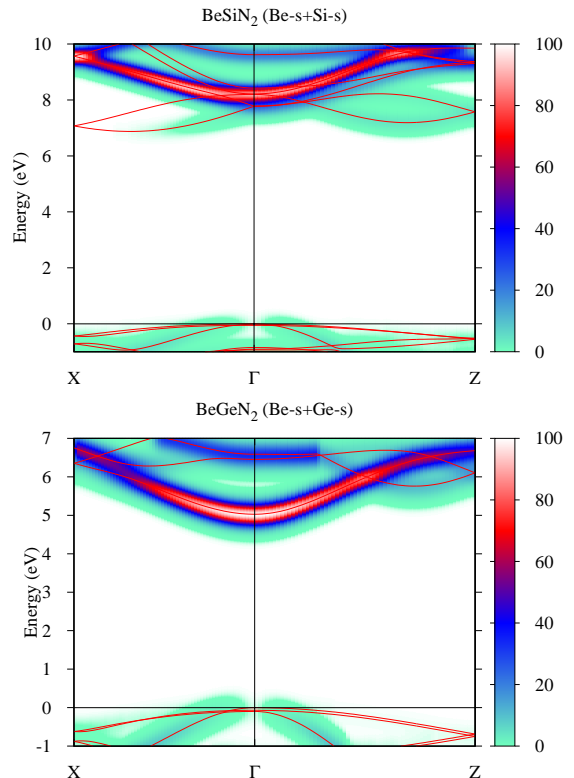


FIG. 4. QSGW band structures near CBM projected on the specified muffin-tin orbital basis functions.

GGA and QSGW calculations. The CBM position is at $2/3$ of the $\Gamma - X$ line irrespective of whether we use the LDA or GGA lattice constants.

To further investigate the origin of the indirect gap in BeSiN₂, we compare it with the band structure of wurtzite BN, which is shown in Fig. 3. Note that wurtzite BN is the most closely related III-N parent compound of the II-IV-N₂ compounds considered here because B is adjacent to Be in the periodic table. We first show it in the standard wurtzite hexagonal Brillouin zone and then in the Brillouin zone corresponding to the orthorhombic $2 \times \sqrt{3} \times 1$ supercell for easier comparison to the II-IV-N₂ materials whose primitive cell corresponds to this supercell of the underlying wurtzite type lattice.

We can understand these relations in terms of band folding. The relation between the hexagonal Brillouin zone and the orthorhombic Brillouin zone is shown in Fig. 3 of Ref. 30. The wurtzite $\Gamma - M$ line is folded in two along the y -direction and becomes the $\Gamma - Y$ direction in the orthorhombic structure. The $\Gamma - K$ is also folded along the x direction but the point K lies at $4\pi/3a_w$ along the x direction and the orthorhombic X about which we fold the bands lies at $\pi/2a_w$. So, the wurtzite w-BN conduction band minimum which occurs at K of the hexagonal Brillouin zone ends up at $2/3 \Gamma - X$ in the orthorhombic Brillouin zone. This is very close to the CBM location also in BeSiN₂.

The band structure of w-BN in the CB is rather com-

plex when folded in the orthorhombic zone and is itself not so well known because w-BN is a rare form of BN. In its tetrahedrally bonded modification which occur at high pressure, the zincblende form has lower energy than the wurtzite. So, we next address the relation between zincblende and wurtzite BN. First, in z-BN, the CBM occurs at X of the fcc Brillouin zone and in w-BN it occurs at K of the hexagonal Brillouin zone. Both of these states are mixtures of s and p -like atomic orbitals and also have a strong component in the interstitial region, in particular the large open channel of wurtzite. A similar situation has recently been pointed out for SiC.³¹ But here we are concerned with the states at Γ . Even in z-BN the p -like Γ_{15c} lies below the s -like Γ_{1c} . In wurtzite, the Γ_{15} splits into Γ_5 (x, y -like) and Γ_1 (z -like) states. So at Γ in w-BN, the conduction band ordering of states is Γ_5 , Γ_1 , and only the third band is the s -like Γ_1 . Now after folding into the orthorhombic BZ, the lowest three conduction bands at Γ all arise from the folding of the $\Gamma - K$ and $\Gamma - M$ bands, the next two, a degenerate and non-degenerate band near about 10-11 eV are derived from the wurtzite Γ_5, Γ_1 B- p -like states and the band a little below 12 eV is the B- s -like state.

Comparing this with BeSiN₂, it becomes clear that here the Γ_5, Γ_1 derived states lie higher than the s -like Γ_1 . This is because the Si- p like states lie at higher energy than B- p like states. The CBM at Γ is a folded state but the next band already has a strong s -like character on both Be and Si. This can be seen in Fig. 4. In this figure we show the band colored according to their weight on muffin-tin orbital basis functions of specific angular momentum character centered on the different atoms. We recognize the typical strongly dispersing mixed cation s -like conduction band in both materials, but while this is the lowest conduction band in BeGeN₂, it lies just a bit higher in the BeSiN₂ case above the folded bands discussed above. Additional colored band structures reflecting their other atomic orbital characters are given in Supplementary Material.³² The CBM has contributions from Be- p , Si- p antibonding with N- s and N- p . This is also clear from the PDOS except that the \mathbf{k} -resolved analysis of the orbital character provides more detailed information. So, in summary, the reason for the indirect band structure and the CBM location in the Brillouin zone is explained by its relation to w-BN parent compound of which we can view BeSiN₂ to be a perturbation. In turn the w-BN band structure is related to that of z-BN by band folding effects. The ordering of these bands depends sensitively on the ordering of atomic s and p -orbitals in the second row of the periodic table elements Be and B and the larger splitting of s and p valence orbitals in Ge than Si.

In BeGeN₂, the conduction band has a stronger dispersion near its minimum at Γ , while the valence bands are quite flat. Nonetheless the lowest conduction band dispersion near its minimum is less pronounced than in MgGeN₂, ZnGeN₂ or CdGeN₂. This is because the Be- s states lie less deep on an absolute scale.

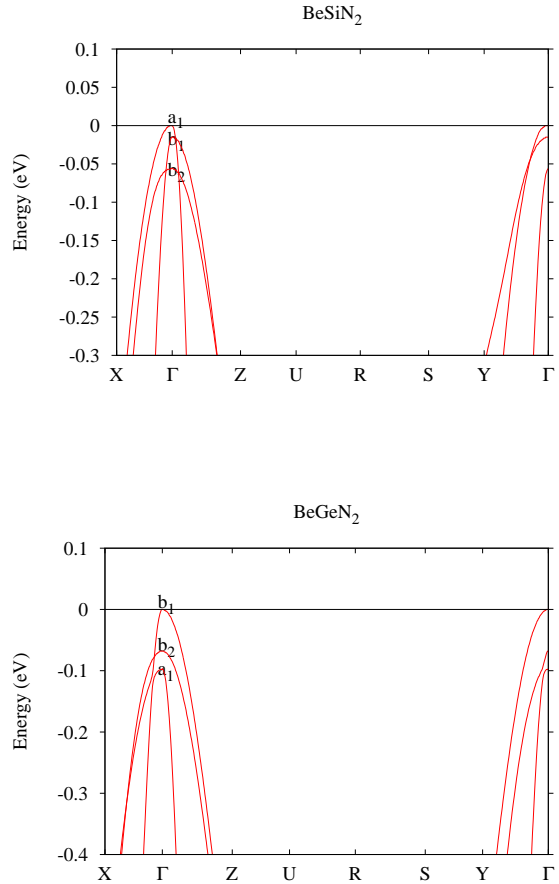


FIG. 5. Band structures near VBM region with symmetry labeling at Γ .

A zoom-in of the electronic band structure near the VBM region for BeSiN₂ and BeGeN₂ is shown in Fig. 5. Here, the energy levels at Γ point are labeled by their related irreducible representation of point group C_{2v} . The states a_1, a_2, b_1, b_2 correspond to basis function z, xy, x, y , respectively. These symmetry labels are helpful to understand whether the optical transitions from the valence bands to the conduction band minimum at Γ point are dipole-allowed or not. In the case of BeGeN₂, the CBM has a_1 symmetry, so the dipole-allowed optical transitions are from a_1 valence states when $E||c$, b_1 when $E||a$, and b_2 when $E||b$, respectively. The crystal field splitting of the energy levels near the VBM at the Γ point are given in Table IV. In both cases, the top three valence bands have a_1, b_1 and b_2 symmetries but they occur in different order in the two compounds. The dispersion of this manifold of three bands near the VBM can be represented by a Kohn-Luttinger type Hamiltonian further discussed in the next section.

The typical automated plotting program only connects the bands according to their band number in terms of in-

creasing energy does not take into account which bands are allowed to cross or not. Therefore to obtain the correct band connectivity a very fine mesh is needed. We here used about 100 points along each direction. We can somewhat further inspect which bands cross or have avoided crossings. For example, for \mathbf{k} along the $\Gamma - X$ direction, the group of \mathbf{k} only contains the identity and the xz mirror plane. Now, b_1 and a_1 are even with respect to this mirror plane but b_2 is odd. Therefore the band emanating from b_2 can cross the one from b_1 but the ones from b_1 and a_1 have an avoided crossing because they are allowed to interact having the same even symmetry. Similarly along $\Gamma - Y$, the remaining group consists of the identity and the yz mirror plane. With respect to this mirror plane a_1 and b_2 are even but b_1 is odd. Therefore we see that the b_2 and a_1 band do not cross.

The band gaps of BeSiN₂ and BeGeN₂ calculated by DFT and 0.8 Σ QSGW at LDA and GGA lattice constants are summarized in Table V. For comparison, the band gaps in w-BN are 7.09 eV (indirect $\Gamma - K$) and 10.76 eV (direct at Γ). For BeGeN₂, the change in the gap from LDA to GGA lattice constants is as expected for tetrahedrally bonded materials: larger lattice constants relaxed in GGA gives rise to smaller band gaps. The change in gap with respect to the unit cell volume can be quantified by the deformation potential, $a_v = d E_g / d \ln V$. The deformation potential of BeSiN₂ is -2.9 eV from finite difference calculation, and for BeGeN₂ is -9.6 eV. The large difference between the two reflects the fact that the orbital character of the CBM is different in both materials. In BeGeN₂, we see that the smaller lattice volume of LDA gives rise to a larger gap already at the DFT level and this is maintained in the QSGW approximation. For BeSiN₂, we give both the lowest indirect gap and the direct gap at Γ . In this case, surprisingly, the QSGW gaps at the GGA lattice constants are slightly larger than those at the LDA lattice constants, even though the lattice constants are larger in GGA. This results from the different orbital character of the CBM in this material. Apparently the deformation potentials of the indirect CBM and even the CBM at Γ states are different from the usual Γ_1 (or a_1 -symmetry) CBM in BeGeN₂ or other II-IV-N₂ materials.

To compare the band gaps of these materials with related III-N and other II-IV-N₂ semiconductors, it is useful to show them in a band gap versus lattice constant diagram as shown in in Fig. 6. The lines here are just guides to the eye and do not include alloy band gap bowing effects. We can see from this plot that these materials fall somewhere in between w-BN and the other III-N or II-IV-N₂ materials.

The direct band gap of BeGeN₂ of 5.03 eV corresponds to a wave length of the emitted or absorbed light of 246 nm in the UV region. The gap is still somewhat lower than in AlN (6.3 eV) but still possibly useful to push LEDs toward deep UV compared with GaN or ZnGeN₂. The gap however is only slightly larger than in MgGeN₂, another direct gap material but occurs at a much smaller

TABLE IV. Energy levels in meV at Γ relative to the VBM at Γ including their symmetry label.

Sym.	BeSiN ₂		Sym.	BeGeN ₂	
		E			E
a_1		0	b_1		0
b_1		-15.0	b_2		-68.0
b_2		-55.8	a_1		-96.6
b_2		-846.3	b_2		-1206.9
a_2		-908.9	a_2		-1311.6

TABLE V. Band gaps (in eV) calculated in the 0.8 Σ QSGW and DFT approximations at the LDA and GGA lattice constants. The second column indicates at which level of theory the band structure is calculated, the third at which level the lattice constant is minimized.

		BeSiN ₂		BeGeN ₂
		indirect	direct	direct
Ref. 6	DFT LDA	5.08	5.7 ^a	5.24 ^b
Ref. 7	DFT LDA	4.95	5.82	3.69
	DFT GGA	5.19	5.93	3.37
This work	DFT LDA	4.96	5.80	4.12
	DFT GGA	5.13	5.95	3.45
	GW LDA	6.82	7.74	5.88
	GW GGA	6.88	7.77	5.03

^a estimated from the band structure figure

^b Their lattice constants are smaller than that in this work

lattice constant, so it will be more difficult to integrate with GaN or ZnGeN₂ in heterostructures. The direct band gap of BeSiN₂ of 7.77 eV corresponds to 159 nm and is even higher than that in AlN but the indirect nature makes it somewhat less attractive for such applications. It might still be a useful material for UV detectors.

D. Effective masses

Finally, we determined the effective masses. As mentioned in the computational section, these include the GW corrections to the bands. The CBM and VBM effective masses are given in Table VI. These correspond to the actual CBM between X and Γ in BeSiN₂ and to the CBM at Γ in BeGeN₂. The effective masses here can be seen to be significantly larger than in ZnGeN₂ or CdGeN₂ or even MgGeN₂. As already mentioned, this corresponds to the lower dispersion of these bands and the less deep Be-*s* atomic energy levels on an absolute scale. The VBM is nearly degenerate but we give here the masses in the three Cartesian directions for the three highest VB states. We can see that for both materials and for each state, there is one direction with a small mass and two with a large mass $m_h > 1.8$. The direction of the small mass is the same in the two materials. In this case of orthorhombic crystal structure, the Cartesian axes coincide

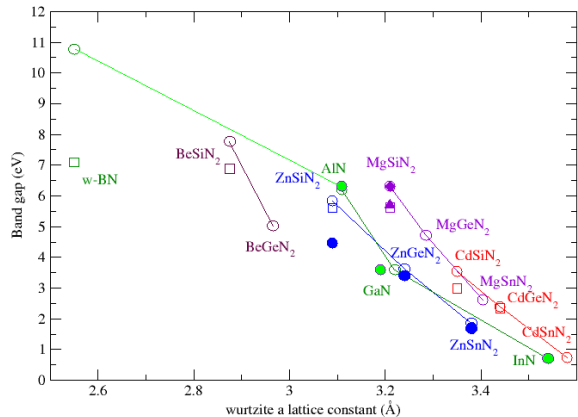


FIG. 6. Band gaps of II-IV-N₂ and III-N compounds. The open and filled symbols represent our calculations and experiment respectively, except for MgSiN₂ where the closed symbol refers to a hybrid functional calculation.³³ The circles represent lowest direct gaps at Γ , the squares indirect gaps.

TABLE VI. Effective mass (in the unit of free electron mass m_e)

	BeSiN ₂	BeGeN ₂
m_x^c	0.54	0.44
m_y^c	0.68	0.54
m_z^c	0.36	0.33
m_x^{a1}	2.59	2.00
m_y^{a1}	2.91	2.03
m_z^{a1}	0.25	0.22
m_x^{b1}	0.37	0.26
m_y^{b1}	4.52	2.09
m_z^{b1}	2.33	1.89
m_x^{b2}	5.77	2.15
m_y^{b2}	0.33	0.27
m_z^{b2}	2.54	1.88

TABLE VII. Parameters of effective Hamiltonian : inverse mass (\hbar^2/m_e)

	BeSiN ₂	BeGeN ₂
A_1	-4.00	-4.55
A_2	3.59	4.01
A_3	0.02	-0.001
B_1	-0.36	-0.50
B_2	-1.17	-1.63
B_3	-0.07	0.04
C_1	-0.02	-0.004
C_2	0.12	-0.03
C_3	1.33	1.65

with crystal axes, i.e., $x = a, y = b, z = c$. The effective masses decrease from BeSiN₂ to BeGeN₂, which is consistent with the trend found in other II-IV-N₂ compounds. The three upper valence bands can be best described by a Luttinger-like effective Hamiltonian.²⁷ The inverse mass parameters in such a Hamiltonian for the three top valence bands in BeSiN₂ and BeGeN₂ are derived from the masses given in Table VI and given in Table VII.

IV. CONCLUSION

In this paper we considered the Be-IV-N₂ compounds, BeSiN₂ and BeGeN₂, of which only the former has been synthesized in the past. This study should be viewed in the context of the until now underexplored broader family of II-IV-N₂ semiconductors. We determined their optimized lattice parameters and internal structural parameters and found them to be in good agreement with previous DFT calculations and the limited available experimental data. Their band structures were determined with the accurate and predictive QSGW method and indicate these materials have gaps in the deep UV. The indirect nature of the band gap of BeSiN₂ is confirmed at the QSGW level. Effective masses were determined as well as band gap deformation potentials and details of the valence band splittings, which are necessary for future exploitation of these materials in heterostructure devices. In a band gap versus lattice constant plot, they fall in a quite well separated area from the other III-N or II-IV-N₂ semiconductors, with a lattice volume closer to those of the ultra wide band gap and extremely hard materials, diamond and tetrahedrally bonded cubic and wurtzite BN. We discussed the relation of their band structure to that of wurtzite BN in terms of band folding, which helps to explain the indirect nature of the gap of BeSiN₂ and the location of its CBM at $2/3 \Gamma - X$.

ACKNOWLEDGMENTS

This work was supported by the National Science Foundation, Division of Materials Research under grant No. 1533957 and the DMREF program. Calculations made use of the High Performance Computing Resource in the Core Facility for Advanced Research Computing at Case Western Reserve University.

-
- ¹ W. R. L. Lambrecht and A. Punya, in *III-Nitride Semiconductors and their Modern Devices*, edited by B. Gill (Oxford University Press, 2013) Chap. 15, pp. 519–585.
- ² A. D. Martinez, A. N. Fioretti, E. S. Toberer, and A. C. Tamboli, *J. Mater. Chem. A* **5**, 11418 (2017).
- ³ S. Lyu, D. Skachkov, E. W. Blanton, K. Kash, and W. R. L. Lambrecht, “Band gaps, band-offsets, disorder, stability region and point defects in ii-iv-n₂ semiconductors,” (2018), submitted to *Phys. Status Solidi(a)* special issue.
- ⁴ P. Eckerlin, A. Rabenau, and H. Nortmann, *Zeitschrift für anorganische und allgemeine Chemie* **353**, 113.
- ⁵ P. Eckerlin, *Zeitschrift für anorganische und allgemeine Chemie* **353**, 225.
- ⁶ J. Y. Huang, L.-C. Tang, and M. H. Lee, *Journal of Physics: Condensed Matter* **13**, 10417 (2001).
- ⁷ V. L. Shaposhnikov, A. V. Krivosheeva, F. A. D’Avitaya, J.-L. Lazzari, and V. E. Borisenko, *physica status solidi (b)* **245**, 142 (2008).
- ⁸ M. van Schilfgaarde, T. Kotani, and S. Faleev, *Phys. Rev. Lett.* **96**, 226402 (2006).
- ⁹ H. B. Schlegel, *J. Comp. Chem.* **3**, 214 (1982).
- ¹⁰ X. Gonze, J. M. Beuken, R. Caracas, F. Detraux, M. Fuchs, G. M. Rignanese, L. Sindic, M. Verstraete, G. Zerah, and F. Jollet, *Computational Materials Science* **25,3**, 478 (2002/11).
- ¹¹ J. P. Perdew, K. Burke, and M. Ernzerhof, *Phys. Rev. Lett.* **77**, 3865 (1996).
- ¹² C. Hartwigsen, S. Goedecker, and J. Hutter, *Phys. Rev. B* **58**, 3641 (1998).
- ¹³ M. Fuchs and M. Scheffler, *Comput. Phys. Commun.* **119**, 67 (1999).
- ¹⁴ W. Kohn and L. J. Sham, *Phys. Rev.* **140**, A1133 (1965).
- ¹⁵ M. Methfessel, M. van Schilfgaarde, and R. A. Casali, in *Electronic Structure and Physical Properties of Solids. The Use of the LMTO Method*, Lecture Notes in Physics, Vol. 535, edited by H. Dreyssé (Berlin Springer Verlag, 2000) p. 114.
- ¹⁶ T. Kotani and M. van Schilfgaarde, *Phys. Rev. B* **81**, 125117 (2010).
- ¹⁷ <http://www.questaal.org/>.
- ¹⁸ T. Kotani, M. van Schilfgaarde, and S. V. Faleev, *Phys. Rev. B* **76**, 165106 (2007).
- ¹⁹ L. Hedin, *Phys. Rev.* **139**, A796 (1965).
- ²⁰ L. Hedin and S. Lundqvist, in *Solid State Physics, Advanced in Research and Applications*, Vol. 23, edited by F. Seitz, D. Turnbull, and H. Ehrenreich (Academic Press, New York, 1969) pp. 1–181.
- ²¹ D. Deguchi, K. Sato, H. Kino, and T. Kotani, *Jap. J. Appl. Phys.* **55**, 051201 (2016).
- ²² C. Bhandari, M. van Schilfgaarde, T. Kotani, and W. R. L. Lambrecht, *Phys. Rev. Materials* **2**, 013807 (2018).
- ²³ B. Cunningham, M. Grüning, P. Azarhoosh, D. Pashov, and M. van Schilfgaarde, *Phys. Rev. Materials* **2**, 034603 (2018).
- ²⁴ M. Shishkin, M. Marsman, and G. Kresse, *Phys. Rev. Lett.* **99**, 246403 (2007).
- ²⁵ W. Chen and A. Pasquarello, *Phys. Rev. B* **92**, 041115 (2015).
- ²⁶ <https://materialsproject.org/>.
- ²⁷ A. Punya, W. R. L. Lambrecht, and M. van Schilfgaarde, *Phys. Rev. B* **84**, 165204 (2011).
- ²⁸ A. P. Jaroenjittichai and W. R. L. Lambrecht, *Phys. Rev. B* **94**, 125201 (2016).
- ²⁹ S. Lyu and W. R. L. Lambrecht, *Phys. Rev. Materials* **1**, 024606 (2017).
- ³⁰ W. R. L. Lambrecht, E. Alldredge, and K. Kim, *Phys. Rev. B* **72**, 155202 (2005).
- ³¹ Y.-i. Matsushita, S. Furuya, and A. Oshiyama, *Phys. Rev. Lett.* **108**, 246404 (2012).
- ³² The supplementary material contains figures of the colored band structures which indicate the atomic orbital character of the bands for BeSiN₂ and BeGeN₂.
- ³³ J. B. Quirk, M. Råsander, C. M. McGilvery, R. Palgrave, and M. A. Moram, *Applied Physics Letters* **105**, 112108 (2014), <http://dx.doi.org/10.1063/1.4896134>.